

A Variable Partial Covering Model for the Seyfert 1 Galaxy MCG-6-30-15

Takehiro MIYAKAWA^{1,2}, Ken EBISAWA^{1,2}, and Hajime INOUE¹

¹*The Institute of Space and Astronautical Science (ISAS), Japan Aerospace Exploration Agency (JAXA),
3-1-1 Yoshinodai, Chuo, Sagami-hara, Kanagawa 252-5210*

²*Department of Astronomy, Graduate School of Science, the University of Tokyo,
7-3-1 Hongo, Bunkyo-ku, Tokyo 113-0033
miyakawa.takehiro@jaxa.jp*

(Received (2010-05-29) ; accepted (2010))

Abstract

We propose a simple spectral model for the Seyfert 1 Galaxy MCG-6-30-15 that can explain most of the 1 – 40 keV spectral variation by change of the partial covering fraction, similar to the one proposed by Miller et al. (2008). Our spectral model is composed of three continuum components; (1) a direct power-law component, (2) a heavily absorbed power-law component by mildly ionized intervening matter, and (3) a cold disk reflection component far from the black hole with moderate solid-angle ($\Omega/2\pi \approx 0.3$) accompanying a narrow fluorescent iron line. The first two components are affected by the surrounding highly ionized thin absorber with $N_H \approx 10^{23.4} \text{cm}^{-2}$ and $\log \xi \approx 3.4$. The heavy absorber in the second component is fragmented into many clouds, each of which is composed of radial zones with different ionization states and column densities, the main body ($N_H \approx 10^{24.2} \text{cm}^{-2}$, $\log \xi \approx 1.6$), the envelope ($N_H \approx 10^{22.1} \text{cm}^{-2}$, $\log \xi \approx 1.9$) and presumably a completely opaque core. These parameters of the ionized absorbers, as well as the intrinsic spectral shape of the X-ray source, are unchanged at all. The central X-ray source is moderately extended, and its luminosity is not significantly variable. The observed flux and spectral variations are mostly explained by variation of the geometrical partial covering fraction of the central source from 0 (uncovered) to ~ 0.63 by the intervening ionized clouds in the line of sight. The ionized iron K-edge of the heavily absorbed component explains most of the seemingly broad line-like feature, a well-known spectral characteristic of MCG-6-30-15. The direct component and the absorbed component anti-correlate, cancelling their variations each other, so that the fractional spectral variation becomes the minimum at the iron energy band; another observational characteristic of MCG-6-30-15 is thus explained.

Key words: galaxies: active – galaxies: individual (MCG-6-30-15) – galaxies: Seyfert – X-rays: galaxies

1. Introduction

The Seyfert 1 galaxy MCG-6-30-15 is the primary “disk-line” target, in which a relativistically broadened iron K-emission line is suggested to originate in the innermost region of the accretion disk around the black hole (e.g., Tanaka et al. 1995). MCG-6-30-15 is also known to exhibit characteristic X-ray spectral variations; Inoue & Matsumoto (2001, 2003), Fabian et al. (2002) and Matsumoto et al. (2003) reported significantly small variability in the iron line energy band of MCG 6-30-15. It is found that the energy-dependent Root Mean Square (RMS) variability is suppressed around the iron line energy, particularly in longer timescales. Inoue and Matsumoto (2001, 2003) proposed that the absorbed spectrum due to photo-ionized warm absorbers mimic shape of the strongly red-shifted iron line, and variation of the warm absorbers may explain the apparently small variability in the iron line energy band.

On the other hand, Miniutti and Fabian (2004) proposed that the suppressed variability in the iron line band may be explained by the general relativistic light-

bending effects, which take place in the very vicinity of the black hole. Miniutti et al. (2007) claim that the Suzaku spectrum of MCG-6-30-15 is in fact consistent with the light-bending model. Niedźwiecki & Życki (2008) and Niedźwiecki & Miyakawa (2010) independently re-examined the light-bending model, and concluded that it is possible to explain the suppressed variability in the iron energy band assuming a particular configuration and movement of the illuminating source. Życki et al. (2010), on the other hand, claim that the light-bending model is not able to explain the Suzaku spectrum, if a broader energy range is adopted than used by Miniutti et al. (2007).

The primary question in MCG-6-30-15 is whether the iron line is truly broad and its little variability is a consequence of the general relativistic light bending effects or not. The critical point to address the problem is to model the underlying continuum spectrum correctly, since the broad iron line parameters are dependent on the choice of the continuum spectral model. In fact, on one hand, Miller, Turner, and Reeves (2008) claim that the “disk-line” is not required, when the continuum spectrum is modeled with multiple warm absorbers. On the other

hand, Reynolds et al. (2009) argue that the absorption-dominated model over-predicts the 6.4 keV fluorescent line emission, and the disk-line model is more physically reasonable. Miller et al. (2009) counterargue that the calculation in Reynolds et al. (2009) neglects opacity at the 6.4 keV line energy, and conclude that variation in the partial-covering fraction may dominate the observed X-ray spectral variability. However, the partial covering scenario by Miller et al. (2009) requires a number of free parameters to model the observed spectrum. Therefore, in order to examine the partial covering scenario, reducing the number of parameters, if possible, and constructing a concrete physical picture to explain the spectral variation is certainly intriguing.

Recently, using the Suzaku data taken in January 2006, Miyakawa et al. (2009) (hereafter Paper I) found a clear correlation between the intensity in the 6 – 10 keV band and the spectral ratio of 0.5 – 3.0 keV / 6 – 10 keV in a time-scale of $\lesssim 10^5$ sec. Essentially the same spectral correlation was confirmed for longer timescales up to ~ 14 years in the RXTE data (Miyakawa 2010). Paper I adopted a spectral model composed of a direct power-law component, its reflection component by a neutral matter (with the solid-angle $\Omega/2\pi \approx 1$), two warm absorbers with different ionization states. The observed spectral variation requires change of the apparent slope of the direct component, whereas the shape and intensity of the reflection component being invariable. A mildly broad iron emission line was required at 6.42 ± 0.06 keV with an intrinsic width of 0.29 keV (1σ) and the equivalent-width 100 eV; such an extremely broadened “disk line” as is claimed by Miniutti et al. (2007) was not required.

In this paper, following Paper I, we attempt to comprehensively understand spectral variability of MCG-6-30-15 using Suzaku and Chandra archival data. Our goal is to find a spectral model which can naturally explain the observed spectral variation of MCG-6-30-15 with a minimum set of free-parameters. If we are successful to construct such a reasonable spectral model, we will see if the relativistically distorted iron emission line is truly present or not in the energy spectrum. We believe this is an important step forward to fully understand X-ray spectral properties of MCG-6-30-15, Seyfert galaxies, and black holes.

2. Observation and Data Reduction

We use the same Suzaku data used in Paper I, taken in 2006 from January 9 to 14th (143 ksec exposure), from 23 to 26 (99 ksec) and from 27 to 30 (97 ksec). We use the XIS data in 1 – 10 keV, and PIN data in 10 – 40 keV. In the present paper, we are interested in spectral variations above 1 keV, so we did not use the data below 1 keV. All of the spectral fits were made with XSPEC v11 (Arnaud 1996). In the following, the xspec model names used in the spectral analysis are explicitly given. A constant factor to adjust normalizations between XIS and PIN is fixed at 1:1.086 (Ishida et al. 2007). For more details about Suzaku data reduction, see Paper I.

The Chandra satellite observed MCG-6-30-15 several times. In this paper, we use the High Energy Transmission Grating Spectrometer (HETGS) data taken between 2004 May 19 and 27, when the source was observed four times resulting in a good exposure time of 522 ksec. For data reduction we used the CIAO 4.0 software package; “tgextract” is used to produce PHA2 spectral files from the Level2 event file. HETGS is composed of High Energy Grating (HEG) and Medium Energy Grating (MEG). The +1 and –1 orders of the HEG were combined, and so were the +1 and –1 orders of the MEG. The HEG and MEG spectra were fitted separately.

Errors quoted in this paper are at statistical 90% confident level.

3. Data Analysis and Results

3.1. Introduction of the “three-component” model

In Paper I, spectral variation of MCG-6-30-15 was studied assuming the “two-component” spectral model given as,

$$F = W_H W_L (N_D + N_R R) P + I_{Fe}, \quad (1)$$

where P is the intrinsic power-law spectrum with a high-energy cut-off (fixed at 160 keV; Guainazzi et al. 1999), N_D is normalization factor of the directly observed component, N_R is normalization factor of the reflected component, R is reflection albedo by the cold optically thick matter (“pexrav” in xspec: Magdziarz & Zdziarski 1995), W_H and W_L represent attenuation by a high- and a low-ionized warm absorbers, respectively, and I_{Fe} is an iron K_α emission line. Effect of interstellar absorption is always taken into account in the spectral fitting (“phabs”; Balucinska-Church & McCammon 1992), but its term is omitted for simplicity in the above expression and hereafter. Amount of the disk reflection is measured with Ω , solid angle of the reflector seen from the central source. Ratio of the normalization of the reflection component to that of the cutoff power-law component corresponds to $\Omega/2\pi$, assuming isotropic emission of the central source.

We used XSTAR Version 2.1kn8 (Kallman et al. 2004) to model the warm absorbers. The temperature, pressure and density of the warm absorbers are assumed to be 10^5 K, $0.03 \text{ dyne cm}^{-2}$ and 10^{12} cm^{-3} , respectively. The incident photo-ionizing spectrum is assumed to be a power-law with the index 2.0, and the solar abundance by Greeves, Noels and Sauval (1996) is adopted for the ionized material. We made a grid model by running XSTAR for different values of ξ and N_H ; the log ξ values are from 0.1 to 5 (erg cm s^{-1}) and the N_H values are from 10^{20} to 10^{24} (cm^{-2}). The number of steps for log ξ and N_H are both 20, thus our grid model has 20×20 grid-points. The redshift of a warm absorber and the source are fixed at 0.001 and 0.00775, respectively (Young et al. 2005, Fisher et al. 1995).

In Paper I, we found that the spectral variation at various timescales is successfully explained by variations of two parameters, normalization factor of the directly observed component (N_D) and apparent slope of the direct

component, such that the slope gets steeper for greater normalizations. The apparent slope change is described by either change of the index of the power-law component (P), ionization state of the low-ionized warm absorber, or column density of the low-ionized warm absorber (W_L).

Below, we scrutinize the spectral model in Paper I carefully, and introduce a more elaborated model. Using the Chandra HETGS, Young et al. (2005) resolved a narrow emission line at 6.4 keV in MCG-6-30-15, which we confirmed via re-analysis of the archival data. The equivalent width of the line is measured as ~ 20 eV, which requires a cold reflector with a solid angle of $\Omega/2\pi \sim 0.3$ viewed from the central X-ray source (e.g., George & Fabian 1991). On the other hand, the best-fit values of N_D and N_R obtained in Paper I indicates that $N_R/N_D = \Omega/2\pi \approx 1$. Consequently, in order to account for the observed disk reflection spectrum of an amount of $\Omega/2\pi \sim 1$ including the outer disk reflection with $\Omega/2\pi \sim 0.3$, we need another disk reflection component or a different spectral component which is similar to disk reflection, corresponding to an amount of $\Omega/2\pi \sim 0.7$.

Thus, we separate the N_R term in (1) into two terms. One is the reflection continuum component from a cold reflector emitting a narrow iron K_α line, solid angle of which is $\Omega/2\pi \sim 0.3$. The other is introduced to represent the remaining part of the N_R term; for this, we adopt a heavily absorbed component by warm absorber, since the absorbed component is similar to the reflection component in shape, and does not have to accompany the fluorescent iron emission line. In fact, a partial covering model has been proposed to explain the continuum spectral shape and variation of MCG-6-30-15 (e.g., Matsuoka et al. 1990; McKernan and Yaqoob 1998; Miller, Turner and Reeves 2008, 2009).

Resultantly, we introduce a new spectral model expressed as

$$F = W_H W_L (N_1 + N_2 W_2) P + N_3 R P + I_{Fe}, \quad (2)$$

where N_1 is normalization of the direct component, N_2 is that for the heavily absorbed component, W_2 stands for another warm absorber that is for the ionized optically thick partial absorber. The normalization factor of the outer reflection component, N_3 is constant and related to the average of N_1 so that $N_3 / \langle N_1 \rangle = \Omega/2\pi \sim 0.3$, and I_{Fe} is a narrow iron emission line with a fixed equivalent width of 20 eV. Hereafter, this model is referred as the ‘‘three-component’’ model.

We try the three-component model to the Suzaku average spectrum in 1 – 40 keV. We found the fit improves if we additionally put a weak iron neutral edge at 7.11 keV and an absorption line at 7.0 keV. The former is considered to be due to a slight difference of the assumed Ω from the exact value, and the latter due to deficiency of the H-like iron absorption line equivalent-width already included in the XSTAR model. Figure 1 and Table 1 show the fitting result for the Suzaku average spectrum with the three-component model in 1 – 40 keV. Parameters of the high-ionized and low-ionized warm absorbers are similar to those in Paper I. For the newly introduced absorption

Table 1. Results of spectral fitting in 1–40 keV for the Suzaku XIS/PIN average spectrum with the three-component model.

<i>Interstellar absorption</i>		
N_H (10^{21} cm $^{-2}$)		$1.5^{+0.4}_{-0.2}$
W_H		
N_H (10^{23} cm $^{-2}$)		$2.4^{+1.8}_{-1.6}$
$\log \xi$		3.37 ± 0.04
W_L		
N_H (10^{21} cm $^{-2}$)		3.7 ± 1.3
$\log \xi$		$1.54^{+0.25}_{-0.13}$
N_1	10^{-2} ph/s/cm 2 at 1 keV	1.44 ± 0.03
N_2	10^{-2} ph/s/cm 2 at 1 keV	0.60 ± 0.09
W_2		
N_H (10^{24} cm $^{-2}$)		$1.6^{+0.6}_{-0.1}$
$\log \xi$		$1.57^{+0.21}_{-0.19}$
P		
photon index		$1.91^{+0.02}_{-0.01}$
E_{cut} (keV)		160(fixed)
N_3		$N_1 \times 0.3$
R^\dagger		
cosIncl		0.866(fixed)
I_{Fe}		
line E (keV)		6.35 (fixed)
sigma (keV)		0.01 (fixed)
norm (10^{-5} ph/s/cm 2)		1.2 ± 0.3
EW (eV)		27 ± 7
edge E (keV)		7.11 (fixed)
MaxTau		0.05 ± 0.02
line E (keV)		7.0 (fixed)
sigma (keV)		0.01(fixed)
norm (10^{-6} ph/s/cm 2)		-6.8 ± 2.4
line E (keV)		2.35 ± 0.02
sigma (keV)		0.01(fixed)
norm (10^{-5} ph/s/cm 2)		-2.3 ± 0.5
reduced chi-square (d.o.f)		1.12 (203)

\dagger ‘‘pexrav’’ model in xspec is used.

component (W_2), we obtain $N_H \sim 1.6 \times 10^{24}$ cm $^{-2}$ and $\log \xi = 1.57$. Normalizations of the heavily absorbed component and the direct component are 0.60 and 1.44 (10^{-2} photons s $^{-1}$ cm $^{-2}$ at 1 keV), respectively, which suggests that the source is partially covered by the ionized thick matter by $0.6/(1.44 + 0.6) \approx 30\%$.

We note that the absorbing matter is marginally Compton thick, so that the Compton scattering may not be negligible for precise spectral calculation (e.g., Yaqoob 1997). This is not considered in the present paper, and will be a subject for future work.

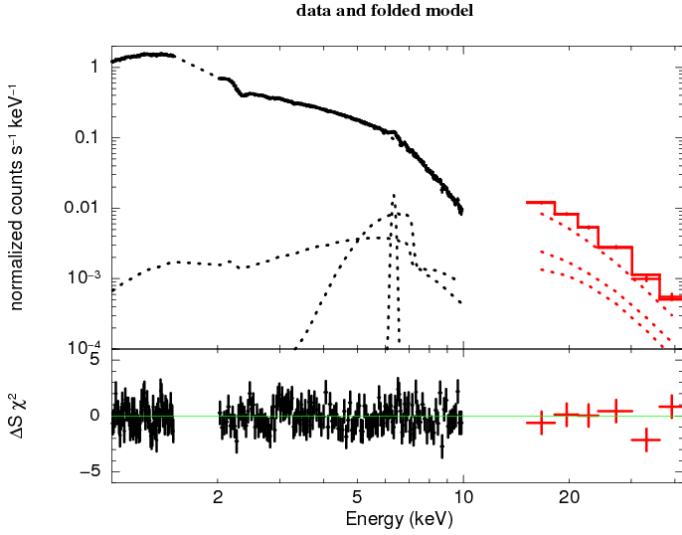


Fig. 1. Spectral fit result for the 1-40 keV average spectrum for Suzaku XIS/PIN with the three-component model.

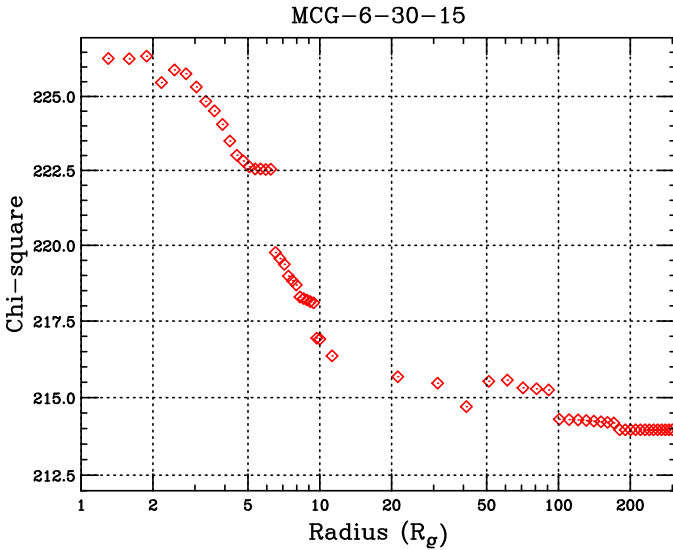


Fig. 2. Chi-squares of fitting to the average spectrum including Laor's disk line model, shown as a function of the inner radius.

Table 2. Results of spectral fitting in 1–40 keV for the average spectrum adding Laor's disk line to the three-component model.

<i>Interstellar absorption</i>	
N_H (10^{21} cm $^{-2}$)	$3.5^{+1.4}_{-0.5}$
<i>Laor's disk-line</i>	
E (keV)	6.40 ± 0.06
Index	–3 (fixed)
r_{in} (R_g)	220^{+180}_{-210}
r_{out} (R_g)	400 (fixed)
inclination (deg)	30 (fixed)
norm (10^{-5})	$1.3^{+0.4}_{-0.6}$
EW (eV)	40 ± 20
W_H	
N_H (10^{23} cm $^{-2}$)	$2.9^{+0.9}_{-0.4}$
log ξ	3.35 ± 0.04
W_L	
N_H (10^{21} cm $^{-2}$)	$3.7^{+1.4}_{-0.8}$
log ξ	$1.52^{+0.21}_{-0.12}$
N_1	
10^{-2} ph/s/cm 2 at 1 keV	$1.44^{+0.04}_{-0.02}$
N_2	
10^{-2} ph/s/cm 2 at 1 keV	$0.55^{+0.05}_{-0.07}$
W_2	
N_H (10^{24} cm $^{-2}$)	$1.7^{+1.3}_{-0.2}$
log ξ	$1.65^{+0.08}_{-0.16}$
P	
photon index	$1.91^{+0.02}_{-0.01}$
E_{cut} (keV)	160 (fixed)
N_3	
	$N_1 \times 0.3$
R^\dagger	
cosIncl	0.866 (fixed)
I_{Fe}	
line E (keV)	6.35 (fixed)
sigma (keV)	0.01 (fixed)
norm (10^{-6} ph/s/cm 2)	$5.4^{+2.4}_{-4.5}$
EW (eV)	12^{+5}_{-10}
edge E (keV)	7.11 (fixed)
MaxTau	0.04 ± 0.02
line E (keV)	7.0 (fixed)
sigma (keV)	0.01 (fixed)
norm (10^{-6} ph/s/cm 2)	$-6.1^{+2.1}_{-2.3}$
line E (keV)	2.35 ± 0.02
sigma (keV)	0.01 (fixed)
norm (10^{-5} ph/s/cm 2)	-2.3 ± 0.5
reduced chi-square (d.o.f)	1.07 (200)

† “pexrav” model in xspec is used.

3.2. Examination of presence of the “disk line”

Several authors claim presence of an extremely broad “disk line” in the energy spectrum of MCG-6-30-15 (e.g., Miniutti et al. 2007). Therefore, we examine if presence of the disk line is reconciled with our three-component model. We analyze the time-average spectrum of MCG-6-30-15 adding a disk line model from a fast-rotating Kerr black hole (Laor 1991). Thus, the model we adopt here has both the narrow line from very far from the black hole, and a putative broad line which is from the region very close to the black hole. We try to fit the spectrum with Laor’s disk line model with varying the inner disk radius, r_{in} .

Table 2 shows the best-fitting result for the Suzaku average spectrum adding Laor’s model to the three-component model, where the fit is slightly improved with $r_{in} \approx 200 r_g$ and the reduced chi-square is 1.07 ($\chi^2/\text{d.o.f} = 214/200$). Note that the additional line is only mildly broadened with $r_{in} \approx 200 r_g$, and the equivalent width of the broad disk line is just 40 ± 20 eV. Figure 2 shows the chi-squares of fitting to the average spectrum as a function of the inner disk radius. As seen from this figure, Δ chi-squares become greater as r_{in} gets less than $\approx 200 r_g$, and it exceeds 2.71 when r_{in} is less than $9 r_g$. Namely, our three-component model is only reconciled with a mildly broad disk line from the region $r_{in} > 9 r_g$ with 90 % confidence.

The reason we do not require a strong, extremely distorted disk line is primarily because that the newly introduced heavily absorbed component in our three-component model (the N_2W_2P term in Equation 2) has an ionized iron edge feature which resembles the broad disk line shape (Figure 1). Secondary reason is that the warm absorbers (W_L and W_H in Equation 2) have spectral curvatures below ~ 5 keV without which the residual may look like a low-energy tail of the disk line. Consequently, we see that the disk line feature is dependent on the choice of the continuum spectral models, and an extremely distorted disk line is not required in our three-component model.

3.3. Spectral fitting for the sliced spectra

Next, we apply the three-component model to the eight “intensity-sliced spectra” (the same spectral sets as used in Paper I) to investigate for spectral variations. The method of creating the intensity-sliced energy spectra is as follows: (1) We created a light curve (the average of XIS0, XIS2, and XIS3), with a bin-width of 128 s in the 0.2–12 keV band. We found that the counting rate varies from ~ 1 to ~ 7 cts s^{-1} . (2) We chose eight time-periods when the source intensity is in the ranges of 1–1.75, 1.75–2.50, 2.50–3.25, 3.25–4.00, 4.00–4.75, 4.75–5.50, 5.50–6.25, 6.25–7.00 cts s^{-1} . These intensity ranges are chosen so that the exposure time for each intensity bin be approximately equal. (3) From the eight time-periods corresponding to the different source flux levels, we created eight intensity-sliced energy spectra (the sum of XIS0, XIS2, and XIS3).

Here, all the parameters are made the same for the

eight spectra except the following three parameters; the direct power-law normalization, N_1 , the absorbed power-law normalization, N_2 , and ionization degree of the low-ionized warm absorber, W_L . Attenuation by a warm absorber is expressed as $W_L \approx \exp(-\sigma(E, \xi) N_{H,L})$, where $\sigma(E, \xi)$ is energy and ionization-degree dependent cross-section and $N_{H,L}$ is the hydrogen column density of the low-ionized absorber. Variation of W_L is due to either a variation of $\sigma(E, \xi)$ or $N_{H,L}$, or both. Here, we investigate two cases, one with a variation of the cross-section $\sigma(E, \xi)$ due to change of the ionization parameter ξ , the other with a variation of $N_{H,L}$.

Eight spectra are fitted simultaneously, and the both cases equally exhibit acceptable fits with reduced chi-square values 1.09 and 0.95 (d.o.f = 1135), respectively. Thus, we could not tell if the ionization parameter or column density of the low-ionized warm absorber is more variable from spectral fitting alone.

When $N_{H,L}$ is fixed, the top and bottom panel of Figure 3 shows the relation between N_1 and $\log \xi$ and that between N_1 and N_2 , respectively. Similarly, when ξ is fixed, the top and bottom panel of Figure 4 shows the relation between N_1 and $N_{H,L}$ and that between N_1 and N_2 , respectively. In either case, correlations between each two of the three parameters are obvious. Note that we see two independent correlations among three free parameters. This indicates that there should be a single principle parameter which is primarily responsible for the observed spectral variations (section 4.1).

3.4. Spectral fitting for Chandra/HETGS data

We have seen that the three-component model is effective to describe the Suzaku spectral variation, and that the ionization degree of the low-ionized warm absorber is variable with intensities. Next, we will see if the three-component model is valid to describe the Chandra HETG spectra and their variations. Strength of Chandra HETG compared to Suzaku is that it can study variation of individual low-energy absorption lines corresponding to change of the ionization degree.

First, we fit the Chandra/HETGS spectra with the three-component model in 1.0–7.5 keV. Since the energy range is much smaller than that of Suzaku, some parameters are not constrained and thus fixed to the Suzaku best-fit values. In Figure 5 and Table 3, we show the fitting result for the average spectrum. We see that the Chandra HETG spectra are successfully modeled with the three-component model with similar parameters to those of Suzaku.

Next, we study possible ionization degree variations in the Chandra/HETGS data by extracting the “bright spectrum” and “faint spectrum” as follows: 1) Create a light curve with a time-bin-width of 128 sec, and calculate average counting rates. 2) Create the “bright spectrum” from the period when the MEG and HEG count rates (0.4–10 keV) are higher than the average, and the “faint spectrum” when the count rates are lower than the average.

We fit the bright/faint spectra in the 1.15–1.55 keV band with a single power-law and two negative gaussians

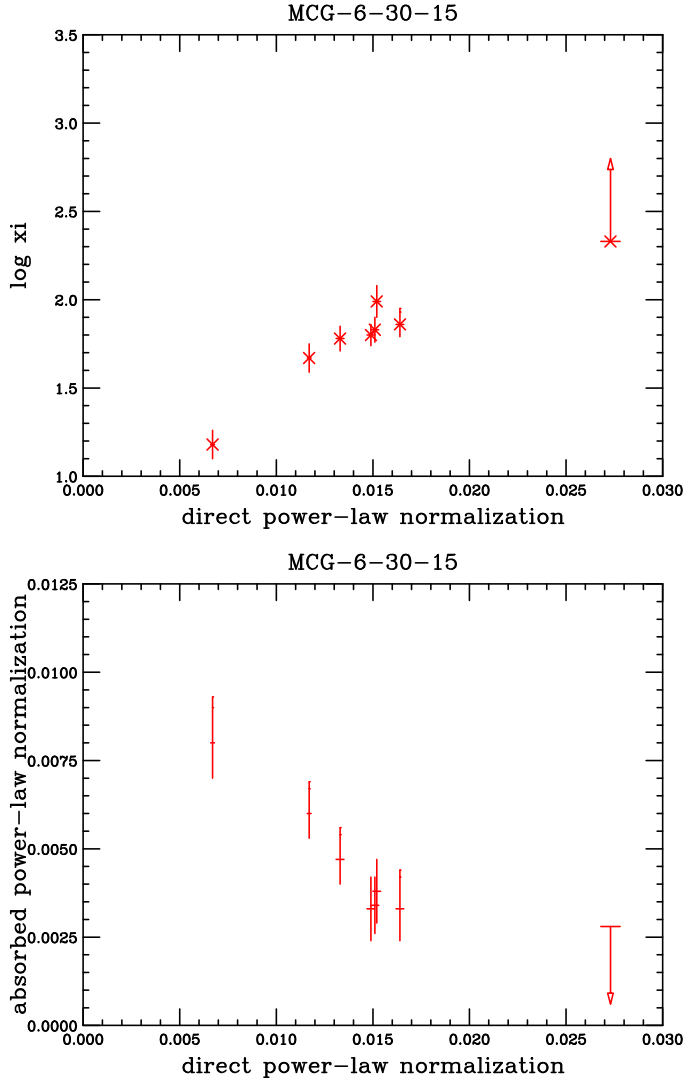


Fig. 3. Correlation among the three parameters, the direct power-law normalization (N_1), ionization parameter of the low-ionized warm absorber (ξ), and the absorbed power-law normalization (N_2), when applying the three-component model to the eight intensity-sliced spectra. (Top) Relation between N_1 and ξ . (Bottom) Relation between N_1 and N_2 .

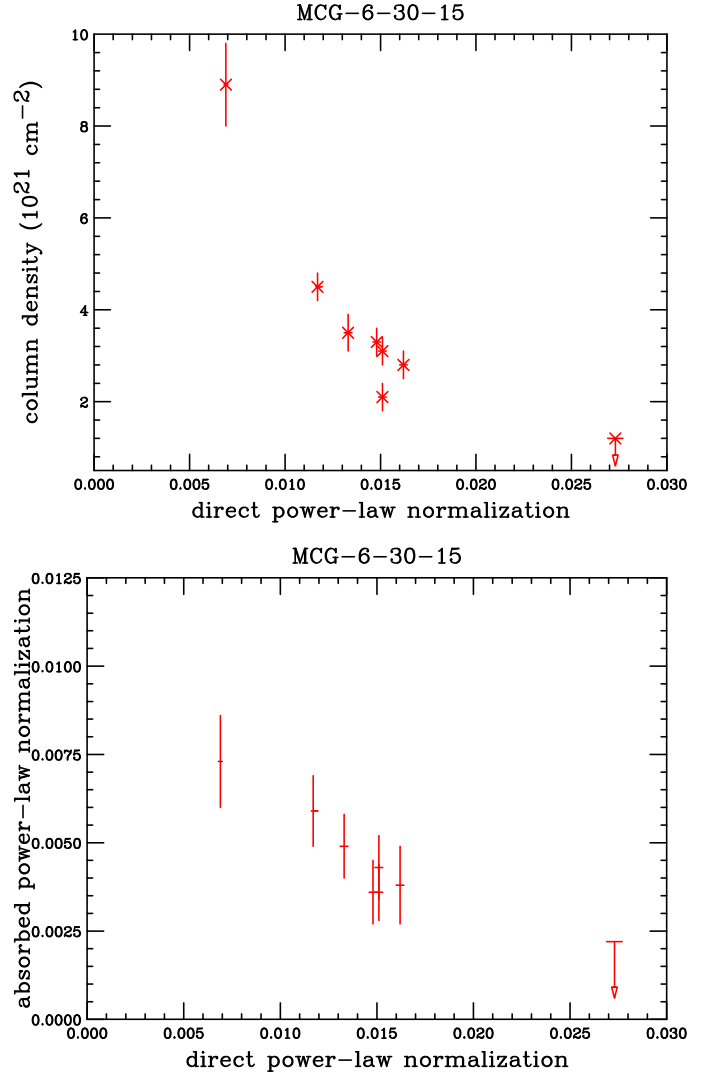


Fig. 4. Correlation among the three parameters, the direct power-law normalization (N_1), column-density of the low-ionized warm absorber ($N_{H,L}$), and the absorbed power-law normalization (N_2), when applying the three-component model to the eight intensity-sliced spectra. (Top) Relation between N_1 and $N_{H,L}$. (Bottom) Relation between N_1 and N_2 .

for the MgXI (He-like 1.34 keV) and MgXII (H-like 1.47 keV) absorption lines. We also fit the bright/faint spectra in the 1.75–2.10 keV band separately with a single power-law and two negative gaussians to investigate for the SiXIII (He-like 1.85–1.86 keV) and SiXIV (H-like 2.00 keV) lines. In Figure 6, we show the fitting result for the bright/faint spectra in both energy bands. We could fit the bright and faint spectra with the common photon index, while only the power-law normalization and the normalization of absorption lines are varied. The best fit parameters are shown in Table 4.

We notice that the MgXI absorption line equivalent width is larger in the faint state, while that of the MgXII line is larger in the bright state. This is understood as due to change of the ionization state of the warm absorber, such that MgXI is more abundant in the faint state, while MgXII is more abundant in the bright state. In fact, ion fraction of MgXI and that of MgXII become equal at $\log \xi \simeq 2$ (e.g., Kallman & Bautista 2001), that is about the best-fit value of the low-ionized warm absorber (Tables 3.4).

As for Si absorption lines, the SiXIII line equivalent width is oppositely larger for the bright spectrum, which is explained by the low-ionized warm absorber with $\log \xi \simeq 2$, since ion fraction of SiXIII increases when $\log \xi$ varies from ~ 1.5 to ~ 2 (Kallman & Bautista 2001). Fraction of SiXIV should increase more dramatically when $\log \xi$ increases accordingly (Kallman & Bautista 2001), but the observed equivalent widths of the SiXIV line is not much different. This result is explained by the presence of the high-ionized warm absorber at $\log \xi \geq 3$, which produces a significant amount of SiXIV but not SiXIII. Consequently, observed variation of the Mg and Si absorption line equivalent-widths is primarily explained by change of the ionization degree of the low-ionized warm absorber according to the flux changes.

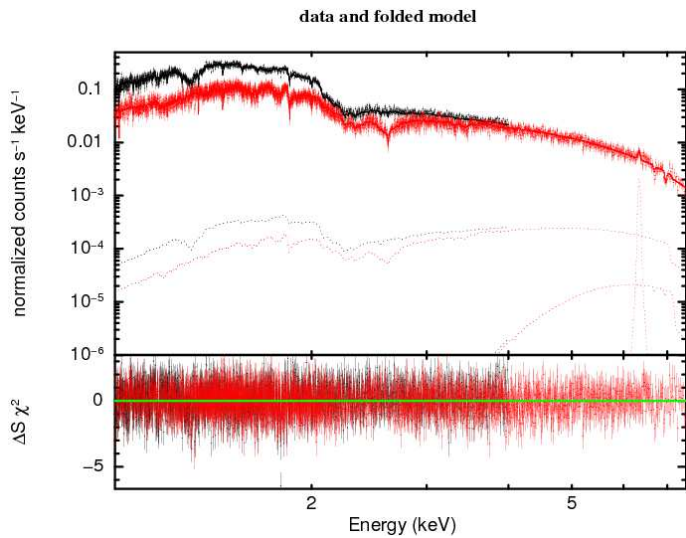


Fig. 5. Spectral fit result for the time-averaged HETGS spectra with the three-component model.

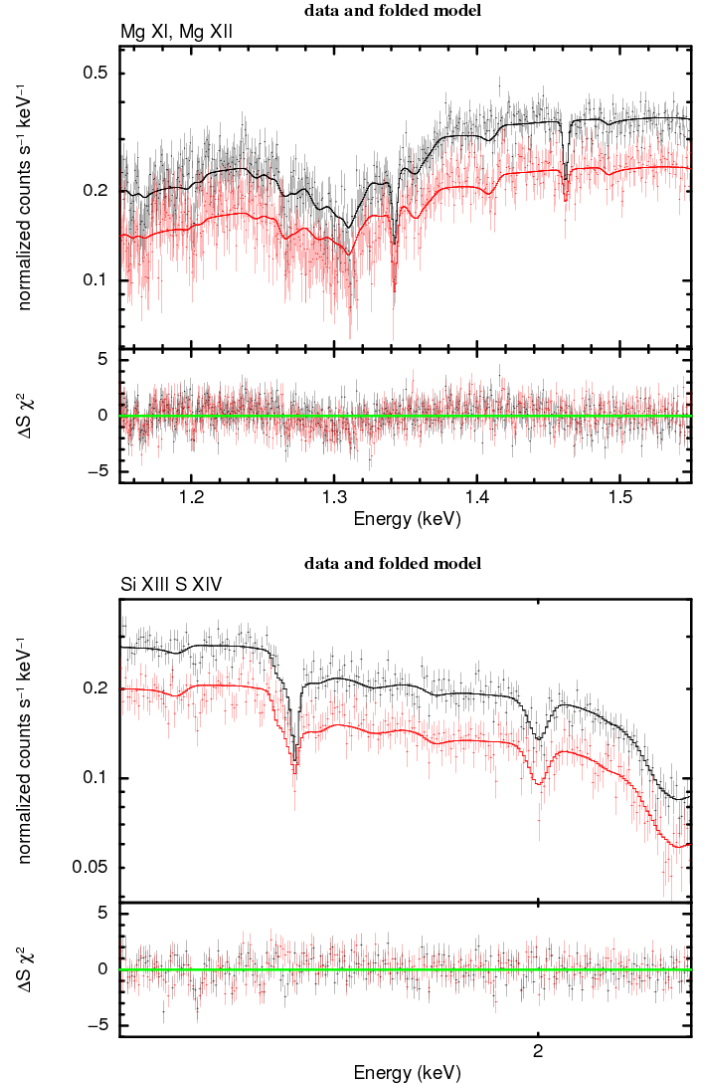


Fig. 6. (Top) Chandra HETGS simultaneous fit in the 1.15–1.55 keV band for the bright spectrum and faint spectrum with a power-law plus two negative gaussian model. Mg absorption lines are at 1.34 keV and 1.47 keV. (Bottom) Simultaneous fit in the 1.75–2.10 keV band with a power-law plus two negative gaussian model. Si absorption lines are at 1.85 keV and 2.00 keV.

We further simultaneously fit the bright/faint spectra in the 1.0–7.5 keV band with the three-component model (Table 5 and 6) by varying normalization of the direct component and ionization degree of the low-ionized warm absorber. In stead of allowing the normalization of the absorbed power-law component to be free, we fixed it to the value of a constant total normalization minus the direct power-law normalization, in order to confirm the anti-correlation between the direct component and absorbed component as observed in Suzaku (Bottom panels in Figures 3 and 4). In Table 5, we show results of allowing the ionization degrees of the low-ionized warm absorber to be free while the column density is fixed; we see the parameter is significantly variable ($\log \xi = 1.95 \pm 0.04$ and

Table 3. Results of spectral fitting of Chandra/HETG in 1–7.5 keV with the three-component model for the average spectrum.

<i>Interstellar absorption</i>		
N_H (10^{21} cm $^{-2}$)	1.5(fixed)	
W_H		
N_H (10^{23} cm $^{-2}$)	2.4(fixed)	
log ξ	3.64 \pm 0.04	
redshift (10^{-3})	1.8 $^{+0.2}_{-0.5}$	
W_L		
N_H (10^{21} cm $^{-2}$)	3.7(fixed)	
log ξ	2.04 \pm 0.03	
redshift (10^{-3})	7.4 \pm 0.1	
N_1		
10^{-2} ph/s/cm 2 at 1 keV	1.23 \pm 0.01	
N_2		
10^{-2} ph/s/cm 2 at 1 keV	<0.2	
W_2		
N_H (10^{24} cm $^{-2}$)	1.6(fixed)	
log ξ	1.57(fixed)	
redshift (10^{-3})	1(fixed)	
P		
photon index	1.76 \pm 0.01	
E_{cut} (keV)	160(fixed)	
N_3		
	$N_1 \times 0.3$	
R^\dagger		
cosIncl	0.866(fixed)	
I_{Fe}		
line E (keV)	6.34 (fixed)	
sigma (keV)	0.018 (fixed)	
norm (10^{-5} ph/s/cm 2)	1.2 \pm 0.4	
EW (eV)	25 \pm 8	
edge E (keV)	7.11 (fixed)	
MaxTau	0.13 $^{+0.10}_{-0.09}$	
line E (keV)	6.98 $^{+0.03}_{-0.06}$	
sigma (keV)	0.01(fixed)	
norm (10^{-6} ph/s/cm 2)	-5.0 $^{+3.9}_{-7.6}$	
reduced chi-square (d.o.f)	0.92 (5099)	

\dagger “pexrav” model in xspec is used.

Table 4. Results of spectral fitting of Chandra/HETGS spectra in 1.15–1.55 keV and 1.75 – 2.10 keV for the intensity sliced spectra when only the power-law normalization and the normalization of absorption lines are varied.

	Bright	Faint
Mg XI absorption line		
line E (keV)	1.3424 \pm 0.0004	
sigma (10^{-3} keV)	1.4 \pm 0.5	
norm (10^{-5} ph/s/cm 2)	-1.2 \pm 0.3	-1.0 \pm 0.2
EW (eV)	-1.9 \pm 0.5	-2.2 \pm 0.4
Mg XII absorption line		
line E (keV)	1.4621 \pm 0.0004	
sigma (10^{-3} keV)	1.2 \pm 0.6	
norm (10^{-5} ph/s/cm 2)	-1.0 \pm 0.2	-0.4 \pm 0.2
EW (eV)	-1.7 \pm 0.3	-1.0 \pm 0.5
photon index	0.95 \pm 0.07	
norm (10^{-3} ph/s/cm 2 at 1 keV)	8.6 \pm 0.2	6.0 \pm 0.2
reduced chi-square	1.21 (χ^2 /d.o.f = 1329/1096)	
	Bright	Faint
Si XIII absorption line		
line E (keV)	1.8515 \pm 0.0005	
sigma (10^{-3} keV)	< 1.7	
norm (10^{-5} ph/s/cm 2)	-1.0 \pm 0.2	0.4 \pm 0.2
EW (eV)	-2.4 \pm 0.5	-1.4 \pm 0.7
Si XIV absorption line		
line E (keV)	2.000 \pm 0.002	
sigma (10^{-3} keV)	5.5 $^{+1.9}_{-2.1}$	
norm (10^{-5} ph/s/cm 2)	-1.5 \pm 0.4	-1.1 \pm 0.4
EW (eV)	-3.8 \pm 1.0	-3.9 \pm 1.4
photon index	0.97 \pm 0.15	
norm (10^{-3} ph/s/cm 2 at 1 keV)	7.7 \pm 0.8	5.7 \pm 0.6
reduced chi-square	1.17 (χ^2 /d.o.f = 539/459)	

1.78 \pm 0.04). Also, ionization degree of the high-ionized warm absorber is made a free parameter, but these values are hardly variable (log ξ = 3.64 \pm 0.05 and 3.62 \pm 0.06).

Because of the presence of constant high-ionized warm absorber, varying column density of the low-ionized warm absorber effectively changes the average ionization states. Therefore, in stead of varying ionization degree of the low-ionized warm absorber, the bright and faint spectral variation can be equally explained by varying its column density. This result is shown in Table 6.

In summary, Chandra/HETGS data confirm that the spectral variation is described by change of only two spectral parameters in the framework of the three-component model (Equation 2), normalization of the direct component (N_1) and either ionization degree or column-density of the low-ionized warm absorber(W_L).

3.5. Time-variation of the spectral parameters and introduction of the “covering fraction”

Next, we create a time-sequence of the energy spectra from Suzaku data, and apply the three-component model. We have made energy spectra every 20 ksec, and performed spectral fits to all the sequential 20 ksec spec-

Table 5. Results of spectral fitting of Chandra/HETG in 1–7.5 keV with the three-component model for the Bright and Faint spectra varying the *ionization parameter* of the low-ionized warm absorber.

	Bright	Faint
<i>Interstellar absorption</i>		
N_H (10^{21} cm $^{-2}$)	1.5(fixed)	
W_H		
N_H (10^{23} cm $^{-2}$)	2.4(fixed)	
log ξ	3.64 \pm 0.05	3.62 \pm 0.06
redshift (10^{-3})	1.82 $^{+0.24}_{-0.29}$	
W_L		
N_H (10^{21} cm $^{-2}$)	3.7(fixed)	
log ξ	1.95 \pm 0.04	1.78 \pm 0.04
redshift (10^{-3})	7.4 \pm 0.2	
N_1		
10^{-2} ph/s/cm 2 at 1 keV	1.47 \pm 0.01	1.05 \pm 0.01
N_2		
10^{-2} ph/s/cm 2 at 1 keV	1.5 – N_1	
W_2		
N_H (10^{24} cm $^{-2}$)	1.6(fixed)	
log ξ	1.57(fixed)	
redshift (10^{-3})	1(fixed)	
P		
photon index	1.78 \pm 0.04	
E_{cut} (keV)	160(fixed)	
N_3		
	$N_1 \times 0.3$	
R^\dagger		
cosIncl	0.866(fixed)	
I_{Fe}		
line E (keV)	6.34 (fixed)	
sigma (keV)	0.018 (fixed)	
norm (10^{-6} ph/s/cm 2)	7.8 \pm 4.3	
EW (eV)	14 \pm 8	18 \pm 10
edge E (keV)	7.11 (fixed)	
MaxTau	0.13 $^{+0.10}_{-0.09}$	
line E (keV)	6.98 $^{+0.03}_{-0.06}$	
sigma (keV)	0.01(fixed)	
norm (10^{-6} ph/s/cm 2)	-5.0 $^{+3.9}_{-7.6}$	
reduced chi-square (d.o.f)	0.89 (7505)	

† “pexrav” model in xspec is used.

Table 6. Results of spectral fitting of Chandra/HETG in 1–7.5 keV with the three-component model for the Bright and Faint spectra varying the *column-density* of the low-ionized warm absorber.

	Bright	Faint
<i>Interstellar absorption</i>		
N_H (10^{21} cm $^{-2}$)	1.5(fixed)	
W_H		
N_H (10^{23} cm $^{-2}$)	2.4 (fixed)	
log ξ	3.65 \pm 0.05	3.62 \pm 0.06
redshift (10^{-3})	1.82 $^{+0.23}_{-0.31}$	
W_L		
N_H (10^{21} cm $^{-2}$)	3.4 \pm 0.4	3.5 \pm 0.4
log ξ	1.54 (fixed)	
redshift (10^{-3})	7.4 \pm 0.2	
N_1		
10^{-2} ph/s/cm 2 at 1 keV	1.57 \pm 0.03	1.11 \pm 0.02
N_2		
10^{-2} ph/s/cm 2 at 1 keV	1.6 – N_1	
W_2		
N_H (10^{24} cm $^{-2}$)	1.6(fixed)	
log ξ	1.57(fixed)	
redshift (10^{-3})	1(fixed)	
P		
photon index	1.83 \pm 0.02	
E_{cut} (keV)	160(fixed)	
N_3		
	$N_1 \times 0.3$	
R^\dagger		
cosIncl	0.866(fixed)	
I_{Fe}		
line E (keV)	6.34 (fixed)	
sigma (keV)	0.018 (fixed)	
norm (10^{-6} ph/s/cm 2)	9.1 \pm 4.3	
EW (eV)	17 \pm 8	22 \pm 10
edge E (keV)	7.11 (fixed)	
MaxTau	0.13 $^{+0.11}_{-0.09}$	
line E (keV)	6.98 $^{+0.04}_{-0.07}$	
sigma (keV)	0.01(fixed)	
norm (10^{-6} ph/s/cm 2)	-10.3 $^{+7.3}_{-7.7}$	
reduced chi-square (d.o.f)	0.91 (7505)	

† “pexrav” model in xspec is used.

tra with the three-component model, to investigate time variation of the spectral parameters. We chose a 20 ksec interval, since variation amplitudes in the 1–10 keV band is maximum at around 20–80 ksec (Inoue, Miyakawa and Ebisawa 2011).

In the spectral fits, N_1 , N_2 and W_L are treated as time-variable in Equation (2). The fits are made for the three observation sequences separately (obsID:700007010, 700007020 and 700007030). We have seen that observed variation of W_L is equally represented with change of the column density $N_{H,L}$ or ionization parameter, ξ (section 3.3). Hereafter, we vary $N_{H,L}$ while ξ is assumed to be invariable throughout the observation. In fact, as we shall see below, variation of $N_{H,L}$ is more physically reasonable than that of ξ .

Figure 7 shows a correlation between N_1 (direct power-law normalization) and N_2 (absorbed power-law normalization), where an inverse correlation is seen between them, as well as in the bottom panels in Figure 3 and 4. The correlation coefficient between N_1 and N_2 is -0.66 . If we fit with a linear relation, $N_2 = a \times N_1 + b$, we obtain $a = -0.58$, $b = 0.01$ and $\chi_r^2 = 1.53$ (d.o.f.=35). On the other hand, fits with a constant N_1 ($N_1 = 0.013$ with $\chi_r^2 = 139.2$ for d.o.f.=36) or N_2 ($N_2 = 0.0063$, $\chi_r^2 = 3.18$ for d.o.f.=36) are not acceptable.

We found that slope of the anti-correlation between N_1 and N_2 is not very far from -1 , which suggests that sum of the two parameters may be rather constant. Therefore, we introduce the “total normalization”, N , as,

$$N \equiv N_1 + N_2. \quad (3)$$

Similarly, we introduce the “covering fraction”, α , as

$$\alpha \equiv \frac{N_2}{N}. \quad (4)$$

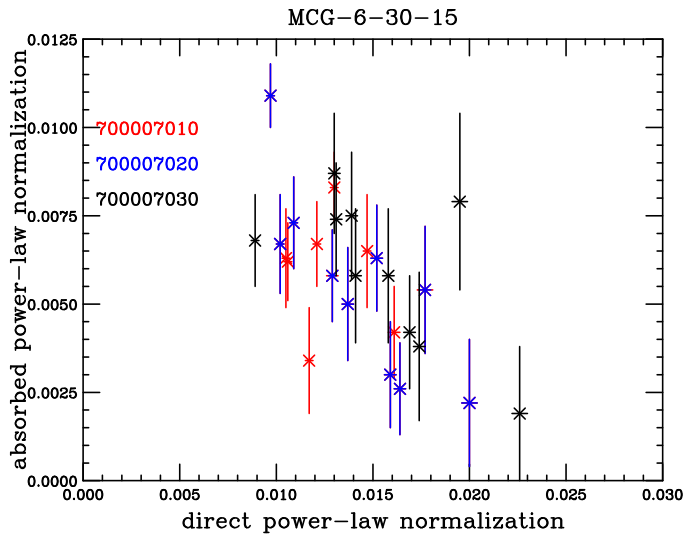


Fig. 7. Correlation between normalizations of the direct component and the absorbed component with the fitting with every 20 ksec.

Obviously,

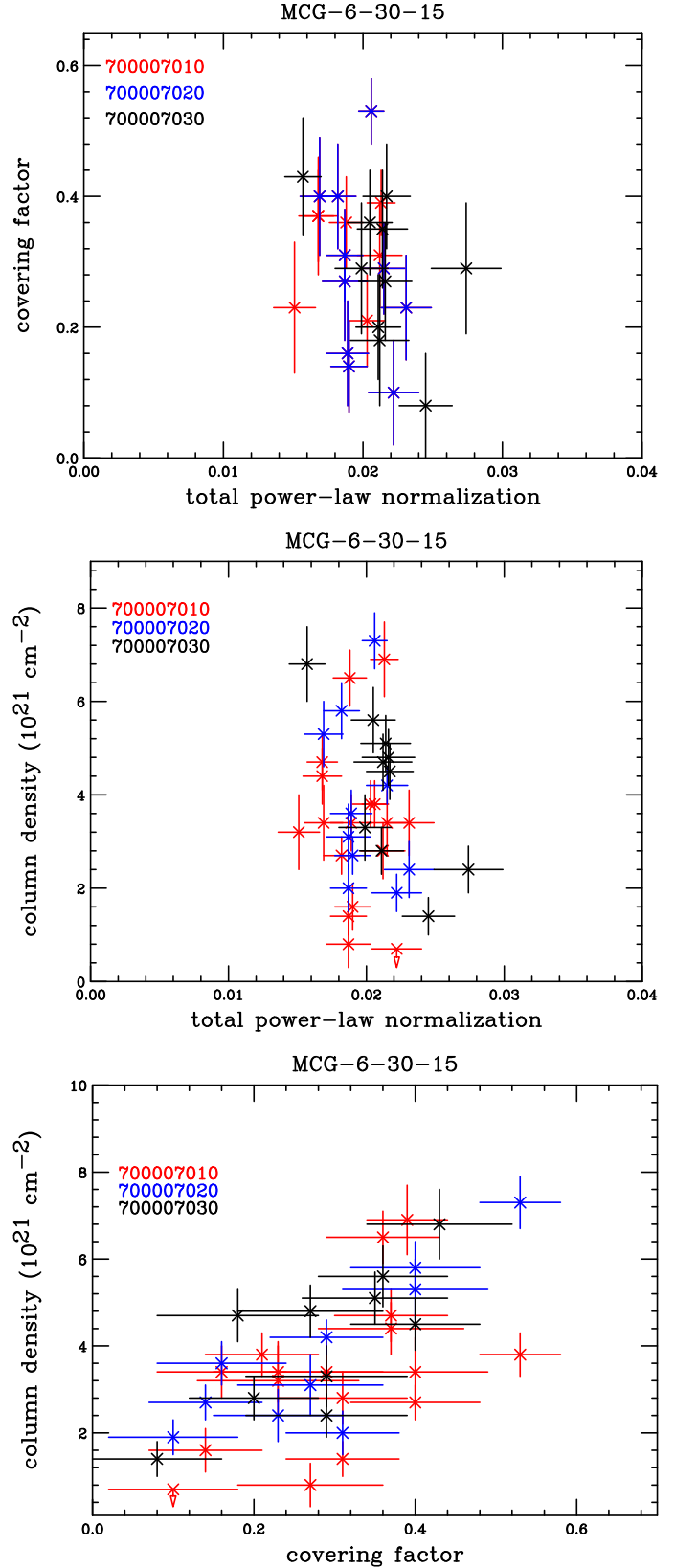


Fig. 8. Correlation among the covering fraction, α , total normalization, N , and column density of the low-ionized warm absorber, $N_{H,L}$ for the spectral fitting for every 20 ksec.

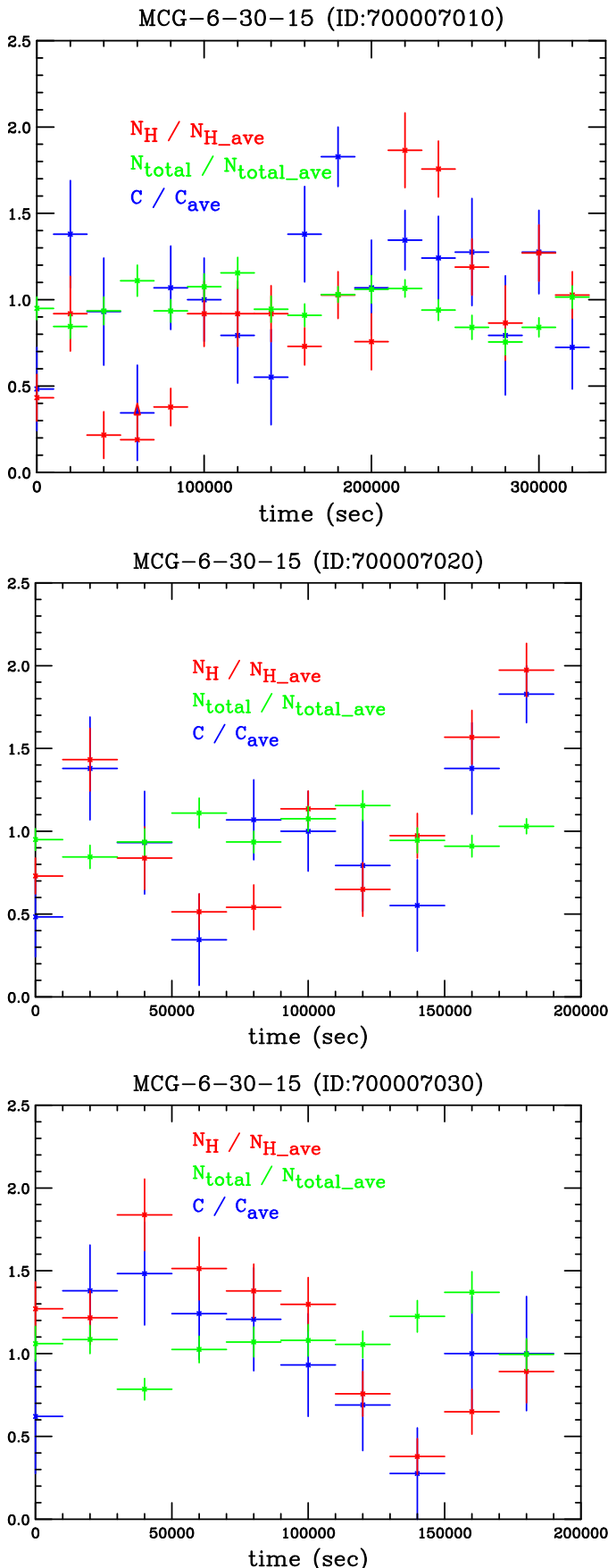


Fig. 9. Fractional variations of the total normalization, N , column density of the lower-ionized warm absorber, $N_{H,L}$, and the covering fraction, α , for every 20 ksec.

Table 7. Variations of and correlations among N , α and $N_{H,L}$ in Figure 8.

x	y	CC [†]	Fitting results		
			$x = \text{const.}(\chi_r^2)$	$y = \text{const.}(\chi_r^2)$	$x = ay + b(\chi_r^2)$
N	α	-0.30	$x = 0.0196(2.35)$	$y = 0.31(2.81)$	$a = -0.003, b = 0.0$
N	$N_{H,L}$	-0.24	$x = 0.0196(2.35)$	N.A.	$a = -0.0001, b = 0.0$
α	$N_{H,L}$	0.64	$x = 0.31(2.81)$	N.A.	$a = 0.04, b = 0.13$

[†]Correlation Coefficient.

$$1 - \alpha = \frac{N_1}{N}, \quad (5)$$

thus, instead of $(N_1, N_2, N_{H,L})$, we can equivalently use $(N, \alpha, N_{H,L})$ to describe the observed spectral variation. In Figure 8, we show correlations among these three parameters.

We study variations of and correlations among the three parameters, $(N, \alpha, N_{H,L})$, by calculating the correlation coefficients between the two, as well as fitting the correlation with a constant parameter or a linear-function. Results are summarized in Table 7. Consequently, we can see a good “orthogonality” between N and α , and N and $N_{H,L}$ (i.e., the fitting parameter a is almost zero, where $N = a\alpha + b$ or $N = aN_{H,L} + b$). Namely, the total power-law normalization N is not significantly variable, while the covering fraction, α , and column-density of the low-ionized absorber, $N_{H,L}$, are more variable. Furthermore, α and $N_{H,L}$ indicate a good correlation with the correlation-coefficient 0.64. Therefore, spectral variation of MCG-6-30-15 at a timescale of 20 ksec is primarily described by a single parameter, either α or $N_{H,L}$. We remind, however, there is a hint of weak anti-correlation between N and α . Further sophistication of the model may explain this correlation (section 4.4.4).

Figure 9 indicates another representation of the spectral parameter variations. As a function of time, the three parameters, $N, \alpha, N_{H,L}$, respectively normalized by their average values, are indicated. The χ_r^2 values around the average (1.0) are 2.4, 2.9 and 10.3 for $N/N_{ave}, \alpha/\alpha_{average}, N_{H,L}/N_{H,L,ave}$ respectively (d.o.f.=36). We can see N is the least variable, while α and $N_{H,L}$ are in sync and more significantly variable. In the following, we will discuss physical meaning of these spectral variations.

4. Discussion

4.1. Variable partial covering Model

We have seen that Suzaku and Chandra energy spectra of MCG-6-30-15 are successfully described by the three-component model introduced with Equation (2). We found N_2 , normalization of the heavily absorbed component, is anti-correlated with normalization of the direct component, N_1 (bottom panels of Figures 3 and 4, and Figure 7). The spectral variation indicates that the “total normalization”, N , (Equation 3) is not so variable, while the covering fraction, α , (Equation 4) and column-density

of the low-ionized warm absorber are in sync and more significantly variable (Figure 8 and 9).

How should we interpret this characteristic spectral variation? Since N_1 and N_2 represent amounts of the non-absorbed and absorbed fluxes emitted from the central X-ray source, respectively, the anti-correlation is naturally understood that a rather constant X-ray source is partially obscured by absorbing matters with variable covering fraction, α . The ‘‘Difference Variation Function analysis’’ introduced by Inoue, Miyakawa and Ebisawa (2011) also confirms that the (N, α) parameter-set is more orthogonal and fundamental than the (N_1, N_2) parameter-set.

Correlation between the low-ionized absorber $N_{H,L}$ and α (bottom panel of Figure 8) is understood as follows: The low-ionized absorber represented by $W_L = \exp(-\sigma(E, \xi) N_{H,L})$ is optically thin (Table 1), so that $W_L \approx 1 - \sigma(E, \xi) N_{H,L}$. On the other hand, the same absorption effect can be expressed by a partial covering model with a fixed column-density as,

$$W_L = 1 - \alpha + \alpha \exp(-\sigma(E, \xi) N_{H,L}^{(fixed)}) \quad (6)$$

$$\approx 1 - \alpha \sigma(E, \xi) N_{H,L}^{(fixed)}. \quad (7)$$

Namely,

$$N_{H,L} = \alpha N_{H,L}^{(fixed)}, \quad (8)$$

that is seen in the bottom panel of Figure 8.

4.2. Explanation of the spectral variation

As we have seen, the observed spectral variation of MCG-6-30-15 is primarily explained by variation of the partial covering fraction, α . Below, we designate our model as the ‘‘variable partial covering model’’. In the framework of the variable partial covering model, the Suzaku intensity-sliced spectra in 1 – 40 keV is explained mostly by change of the covering fraction. Using the total normalization N and the covering fraction α , our three-component model (2) is rewritten as follows:

$$F = W_H W_L (1 - \alpha + \alpha W_2) NP + N_3 RP + I_{Fe}. \quad (9)$$

In Equations (8) and (9), only variable parameters are α and N . In Figure 10 and Table 8, we show an example of the simultaneous fit of the Suzaku intensity-sliced spectra with variable α (the same dataset as used in section 3.3). The eight intensity-sliced spectra are successfully fitted with the constant normalization, $N = 1.80 \times 10^{-2}$ photons $\text{s}^{-1} \text{cm}^{-2}$ at 1 keV (except the brightest one where N is 1.5 times higher), while α is variable from 0.63 (dimmiest) to null (brightest).

4.3. Explanation of the small variability in the iron energy band

The well-known small variability in the iron energy band (Section 1) is also nicely explained in the framework of the variable partial covering model. In order to see energy dependence of the variation at a specific timescale, we took the following method to calculate the ‘‘Difference Variation Function’’, $DVF(E)$ (Inoue, Miyakawa and

Ebisawa 2011): (1) We choose a time-interval of interest, t , to investigate for spectral variations; here, we take $t = 40$ ksec. (2) Energy spectra are calculated for every $t/2$, namely, 20 ksec. (3) For every two contiguous energy spectra, we recognize the ‘‘brighter spectrum’’ and the ‘‘fainter spectrum’’, $B(E)$ and $F(E)$, respectively. (4) We average all the brighter spectra and all the fainter spectra. (5) Thus, for a given time-period t , we create a single ‘‘averaged bright spectrum’’ $\langle B(E) \rangle$ and a single ‘‘averaged faint spectrum’’ $\langle F(E) \rangle$. (6) We calculate difference of the averaged bright spectrum and the averaged faint spectrum relative to the average, as

$$DVF(E) \equiv \frac{\langle B(E) \rangle - \langle F(E) \rangle}{\langle B(E) \rangle + \langle F(E) \rangle}. \quad (10)$$

In Figure 11, we show the Difference Variation Function thus calculated at a timescale of 40 ksec. Together, we show a model prediction of the Difference Variation Function calculated in the framework of the variable partial covering model (Eq. 29 in Inoue, Miyakawa and Ebisawa 2011), where the covering fraction α is assumed to be the major variable parameter, while the total normalization N adds minor fluctuation. Agreement of the observation and model calculation is obvious.

4.4. Parameters of the warm absorbers

Next, we estimate physical parameters of the warm absorbers in Equation (9), W_H , W_L and W_2 , which are high-ionized warm absorber, thin low-ionized warm absorber and thick partial absorber, respectively. We provide suffixes, H, L and 2 to distinguish column densities and ionization parameters of these warm absorbers. In the following, r is distance from the central X-ray source to the absorber, h is a representative thickness of the absorbing region along the line of sight, and n is density.

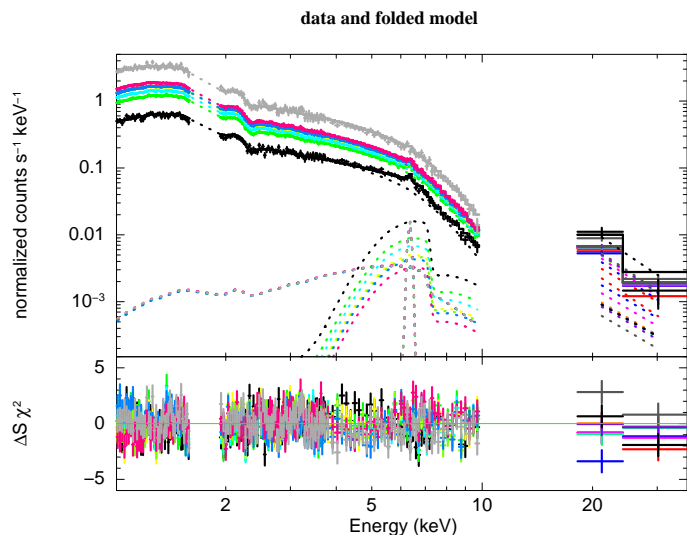


Fig. 10. Suzaku intensity-sliced spectra simultaneously fitted with varying only the covering fraction. All the other parameters fixed, except the brightest spectrum where the total normalization is 1.5 times greater than the others.

Table 8. Results of spectral fitting in 1–40 keV for the intensity-sliced spectra when only the covering fraction is varied (from slice 1 to 8, the dimmest to the brightest).

state	slice 1	slice 2	slice 3	slice 4	slice 5	slice 6	slice 7	slice 8
<i>Interstellar absorption</i>								
N_H (10^{21} cm $^{-2}$)	1.9±0.1							
W_H								
N_H (10^{23} cm $^{-2}$)	2.4 (fixed)							
log ξ	3.43±0.03							
<i>Covering Fraction</i>								
α	0.632	0.356	0.269	0.195	0.181	0.166	0.122	< 0.1
W_L								
$N_{H,L}^{(fixed)}$ (10^{22} cm $^{-2}$)	1.3							
N_H	$\alpha N_{H,L}^{(fixed)}$							
log ξ	1.88±0.03							
N								
10^{-2} ph/s/cm 2 at 1 keV	1.80							
N_1	2.71							
N_2	$(1 - \alpha) N$							
N_2	αN							
W_2								
N_H (10^{24} cm $^{-2}$)	1.6 (fixed)							
log ξ	1.63±0.05							
P								
photon index	1.88±0.01							
E_{cut} (keV)	160 (fixed)							
N_3								
pextrav K (10^{-3})	$0.3 \times N_1$ (for slice5)							
R^\dagger								
cosIncl	0.866 (fixed)							
I_{Fe}								
line E (keV)	6.35 (fixed)							
sigma (keV)	0.01 (fixed)							
norm (10^{-5} ph/s/cm 2)	1.4±0.2							
edge E (keV)	7.11 (fixed)							
MaxTau	0.08±0.01							
line E (keV)	7.0 (fixed)							
sigma (keV)	0.01 (fixed)							
norm (10^{-6} ph/s/cm 2)	-4.8±1.7							
line E (keV)	2.35±0.01							
sigma (keV)	0.01 (fixed)							
norm (10^{-5} ph/s/cm 2)	-1.9±0.3							
Reduced chisq (d.o.f)	0.49 (1149)							

† “pextrav” model in xspec is used.

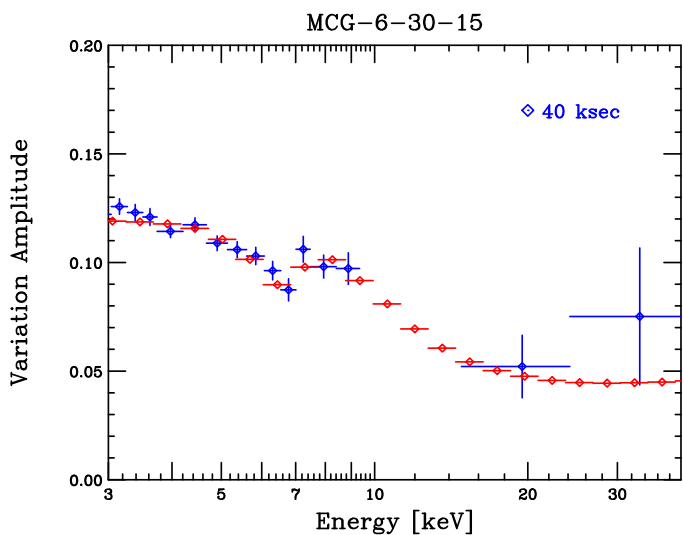


Fig. 11. Energy dependence of the spectral variation (“Difference Variation Function”; blue) and model simulation (red) in the framework of the variable partial covering model. This figure is the same one as Figure 4 in Inoue, Miyakawa and Ebisawa (2011).

First, in general, we note the following relations hold:

$$\xi \equiv L/nr^2 = \frac{L}{N_H r} \left(\frac{h}{r} \right), \text{ where } N_H = nh, \quad (11)$$

$$r = \frac{L}{N_H \xi} \left(\frac{h}{r} \right) \leq \frac{L}{N_H \xi}. \quad (12)$$

For the luminosity, we take the representative value 10^{43} erg/s, which is valid for order estimation, since the flux variation is much less than an order of magnitude.

4.4.1. High-ionized warm absorber, W_H

From model fitting (Table 8), $\xi_H \simeq 10^{3.4}$ erg cm/s, $N_{H,H} \simeq 10^{23.4}$ cm $^{-2}$. Hence,

$$r_H = \frac{L}{N_{H,H} \xi_H} \left(\frac{h_H}{r_H} \right) \leq \frac{L}{N_{H,H} \xi_H} \simeq 10^{16.2} \text{ cm}. \quad (13)$$

Our analysis has indicated that the high-ionized warm absorber is constant, while partial covering fraction is variable. This suggests the variable partial absorbers be embedded in the largely extended, static high-ionized warm absorber. Hence, we assume $h_H \sim r_H$, and take $r_H \sim 10^{16}$ cm and $n_H \sim 10^7$ cm $^{-3}$ for typical parameters of the high-ionized warm absorbers.

4.4.2. Thick partial absorber, W_2

From model fitting (Table 8), $\xi_2 \simeq 10^{1.6}$ erg cm/s, $N_{H,2} \simeq 10^{24.2}$ cm $^{-2}$. Hence,

$$r_2 \simeq \frac{L}{N_{H,2}\xi_2} \left(\frac{h_2}{r_2} \right) \leq \frac{L}{N_{H,2}\xi_2} \simeq 10^{17.2} \text{ cm.} \quad (14)$$

Here, we may further constrain the parameters of the partial absorber from variation timescale of the partially absorbed component. In our variable partial covering model, typical variation timescale ($\sim 10^5$ sec; Figure 9) corresponds to the crossing time of the X-ray absorbing clouds in front of the X-ray source. We will call these clouds as the “low-ionized clouds”, hereafter. Assuming that size of the X-ray source and that of a low-ionized cloud have similar dimensions, the crossing timescale is expressed as $\sim h_2/V$, where V is the velocity of a low-ionized cloud. Hence,

$$h_2 \sim V \times 10^5 \sim 10^{14} \left(\frac{V}{10^9 \text{ cm/s}} \right) \text{ cm,} \quad (15)$$

where V is normalized to a typical velocity of the broad line region (BLR) clouds. Combining h_2 and $N_{H,2} \approx 10^{24}$ cm $^{-2}$, we estimate parameters of the partial absorbers as follows:

$$r_2 \simeq \left(\frac{L}{\xi_2 N_{H,2}} h_2 \right)^{1/2} \simeq 10^{15.7} \text{ cm,} \quad (16)$$

$$n_2 \sim 10^{10} \text{ cm}^{-3}. \quad (17)$$

Note that a low-ionized cloud may have internal ionization structures, which we will see below.

4.4.3. Thin low-ionized warm absorber, W_L

In our variable partial covering model, the low-ionized warm absorber (W_L) and the partial absorber (W_2) are closely associated. Presumably, they are different parts of the low-ionized clouds. We point out that presence of such internal structures in the BLR clouds is also suggested in Mrk 766 (Risaliti et al. 2011).

In our model, the low-ionized warm absorber has a fixed column-density $N_{H,L}^{(fixed)}$ with a variable partial covering factor (Equation 8); we simply write this column density as $N_{H,L}$ below. From model fitting (Table 8), $N_{H,L} \sim 10^{22.1}$ cm $^{-2}$ and $\xi_L \simeq 10^{1.9}$ erg cm/s.

If we take the distance of the low-ionized clouds r_2 ,

$$n_L = \frac{L}{\xi_L r_2^2} \simeq 10^{9.7} \text{ cm}^{-3}, \quad (18)$$

$$h_L = N_{H,L}/n_L \simeq 10^{12.4} \text{ cm.} \quad (19)$$

Note that values of n_L and ξ_L are between those of the high-ionized absorber ($n_H \sim 10^7$ cm $^{-3}$ and $\xi_H \sim 10^{3.4}$) and the partial absorber ($n_2 \sim 10^{10}$ cm $^{-2}$ and $\xi_2 \sim 10^{1.6}$), respectively. The thickness h_L is much smaller than that of the partial absorber $h_2 \sim 10^{14}$ cm. Therefore, the low-ionized absorber is considered to be in the boundary layer between the low-ionized cloud and the high-ionized warm absorber. We may call this putative layer as the “cloud envelope”.

Meanwhile, it is known that there takes place thermal instability in the range of $\xi = 10^2 \sim 10^3$ erg cm/s (Reynolds & Fabian 1995). Therefore, it is reasonable that the cloud envelope continuously connects the partial absorber in the low-ionized cloud and the surrounding constant high-ionized warm absorber.

4.4.4. Putative X-ray blocker

We notice the Thomson optical depth ($\sim N_H/10^{24.2}$) of the partial absorber is about unity. Presumably, this is not just a coincidence, but suggests that the low-ionized cloud has internal density gradients extending up to more than unit Thomson optical depth, such that attenuation with continuously different optical depths is approximated by unit Thomson optical depth. Thus, the low-ionized cloud may well have central, cold Thomson thick cores ($N_H \geq 10^{24.2}$ cm $^{-2}$), which are completely opaque to incoming X-rays. We may not see these “X-ray blockers” directly, but if we take into account the effect of the X-ray blockers, the weak anti-correlation between the total normalization N and the covering fraction α (top-panels of Figure 8) might be explained.

4.5. Origin of the Variable Partial Covering

Finally, we present a physical picture surrounding the X-ray source to explain the observations. In Table 9, we summarize parameters of the absorbers in our model. Basic points of our variable partial covering model are the following:

1. Observed X-ray flux and spectral variability is primarily caused by random passages of the low-ionized clouds in front of the central X-ray source. A typical size of each low-ionized cloud is $h_2 \sim 10^{14}$ cm and a typical velocity is $V \sim 10^9$ cm/s (Equation 15).
2. Central X-ray source is not always fully blocked, nor fully exposed. The covering fraction is variable between null to ~ 0.6 (Table 8), and it fluctuates by an amplitude of ~ 50 % (Figure 9).

We may estimate the average covering fraction C_{ave} from intensity-sliced spectra as $C_{ave} = \sum_{i=1}^8 C_i \times t_i/T$, where t_i and T are exposure time for each spectrum and the total observation, respectively. We thereby obtain $C_{ave} \sim 0.3$. The integrated covering fraction is considered to be about 0.1 for BLR (e.g., Blandford et al. 1991). Thus, our results suggest that the partial absorption takes place in the BLR, and the low-ionized clouds corresponds to the BLR blobs.

We may estimate number of the absorbing clouds in the field of view, N_{cloud} , and size of the central X-ray source, r_x , as follows. Assuming that fluctuation of the covering fraction, ≈ 0.5 , is determined by statistical fluctuation of the number of clouds, $\Delta N_{cloud}/N_{cloud}$, N_{cloud} is estimated as ≈ 4 . The average covering fraction, ≈ 0.3 , may be written as $N_{cloud}\pi(h_2/2)^2/\pi r_x^2$, thus, $r_x \approx 2h_2 \approx 2 \times 10^{14}$ cm.

Typically, BLR blobs have a velocity of $V \sim 10^9$ cm/sec. Assuming the Kepler velocity has a similar value, $r = (c^2/2V^2)r_s \sim 500 r_s$, where r_s is the Schwarzschild radius.

Table 9. Summary of Parameters of the Absorbers

Absorbers		r [cm]	$\log N_H$	$\log \xi$	h [cm]	n [cm ⁻³]
High-ionized warm absorber, W_H		10^{16}	23.4	3.4	10^{16}	10^7
Low-ionized cloud	Envelope	$10^{15.7}$	22.1	1.9	$10^{12.4}$	$10^{9.7}$
	Main body					
	Core					
Thin low-ionized warm absorber, W_L		$10^{15.7}$	24.2	1.6	10^{14}	10^{10}
Thick partial absorber, W_2						
X-ray Blocker						
			≥ 24.2	≤ 1.6	$\approx 10^{14}$	$\geq 10^{10}$

Identifying this with $r_2 \sim 10^{15.7}$ cm (Equation 16), the central black hole mass of MCG-6-30-15 is $\sim 3 \times 10^7 M_\odot$. Thus, the central X-ray source ($r_x \sim 2 \times 10^{14}$ cm) is extended to $\sim 20 r_s$ around the black hole. Besides variation of the BLR clouds, the X-ray source is variable on a timescale down to ~ 1 ksec (Inoue, Miyakawa and Ebisawa 2011), which may be compared with the free fall time, $r/\sqrt{\frac{GM}{r}}$. Then, the intrinsic source variation arises at a few times the Schwarzschild radius, around the innermost stable circular orbit.

We point out that solid angle of the low-ionized clouds seen from the X-ray source should be much smaller than 4π , otherwise we will have to see strong fluorescent lines from the clouds. If a thick absorber with $N_H \gtrsim 10^{24}$ cm⁻² covers the power-law component completely ($\Omega \sim 4\pi$), equivalent width of the iron line to the reflection component is ~ 1 keV. Considering $C_{ave} \sim 0.3$ and the ratio of the reflection component to the direct component, 10 to 1, the expected iron line equivalent width is ~ 30 eV. As mentioned in subsection 5.5.2, we found the fit improves if a mildly broad disk-line is added, where the best-fit inner radius and the equivalent width are $\gtrsim 200 r_g$ and 40 ± 20 eV, respectively (Table 2). These mildly broadened, weak iron emission lines may well be expected from fluorescence in the BLR clouds.

Figure 12 gives a schematic view of internal structure of the low-ionized cloud and the variable partial covering model surrounding the black hole. The low-ionized cloud (BLR cloud) has internal ionization structure. A putative blocker in the core would block the incoming X-rays completely. The main body of the low-ionized cloud is the thick partial absorber surrounding the core. Still the outer cloud envelope corresponds to the thin low-ionized warm absorber. Central X-ray emission region around the black hole is mildly extended, and partially covered by these low-ionized clouds. Variation of the covering fraction explains most of the observed flux and spectral variations.

Finally we comment that the idea of partial covering is not new for MCG-6-30-15 to explain its spectral shape and variation (e.g., Matsuoka et al. 1990; McKernan and Yaqoob 1998; Miller, Turner and Reeves 2008, 2009). Recently, similar partial covering models are proposed to explain spectral variations of NGC 3516 (Turner et al. 2008), Mrk 766 (Risaliti et al. 2011) and other Seyfert galaxies (Turner & Miller 2009). Presumably, partial covering of rather constant X-ray source is a common mechanism in Seyfert galaxies. It is of interest to study spectral

variations of Seyfert galaxies systematically to see if the observed X-ray variability is truly due to intrinsic luminosity variation or explained by partial covering of the constant source.

5. Conclusion

We have analyzed Suzaku and Chandra archival data of MCG-6-30-15 and constructed a new model to explain the observed spectral variation. Our main conclusions are summarized below:

1. We have shown that the observed energy spectra and spectral variation can be explained by the “three-component model” (Equation 2) that includes (1) a direct power-law component, (2) a heavily absorbed power-law component by thick photoionized material, and (3) a cold disk reflection component far from the black hole. The first two components are affected by two warm absorbers having different ionization states.
2. The ionized iron K-edge of the heavily absorbed component and spectral curvature due to the warm absorbers explain most of the seemingly broad “disk line” spectral feature. Consequently, general relativistic interpretation of the broad iron emission line feature in MCG-6-30-15 is not confirmed. The claim that MCG-6-30-15 is a Kerr black hole with nearly extreme rotation assuming the relativistic line-broadening (e.g., Miniutti et al. 2007) is questionable.
3. We propose the “variable partial covering model”, in which a central, moderately extended X-ray source is partially covered by variable low-ionized clouds in the line of sight. In this model, observed X-ray spectral variation is primarily caused by change of the partial covering fraction of the central source. These absorbing clouds presumably correspond to the fast-moving broad line region (BLR) clouds.

The authors would like to thank Profs. P. Życki, Y. Terashima, Y. Ueda and K. Makishima for fruitful discussion. This research has made use of public Suzaku data obtained through the Data ARchives and Transmission System (DARTS), provided by the Institute of Space and Astronautical Science (ISAS) at Japan Aerospace Exploration Agency (JAXA), public Chandra data obtained through the High Energy Astrophysics Science Archive Research Center (HEASARC) at

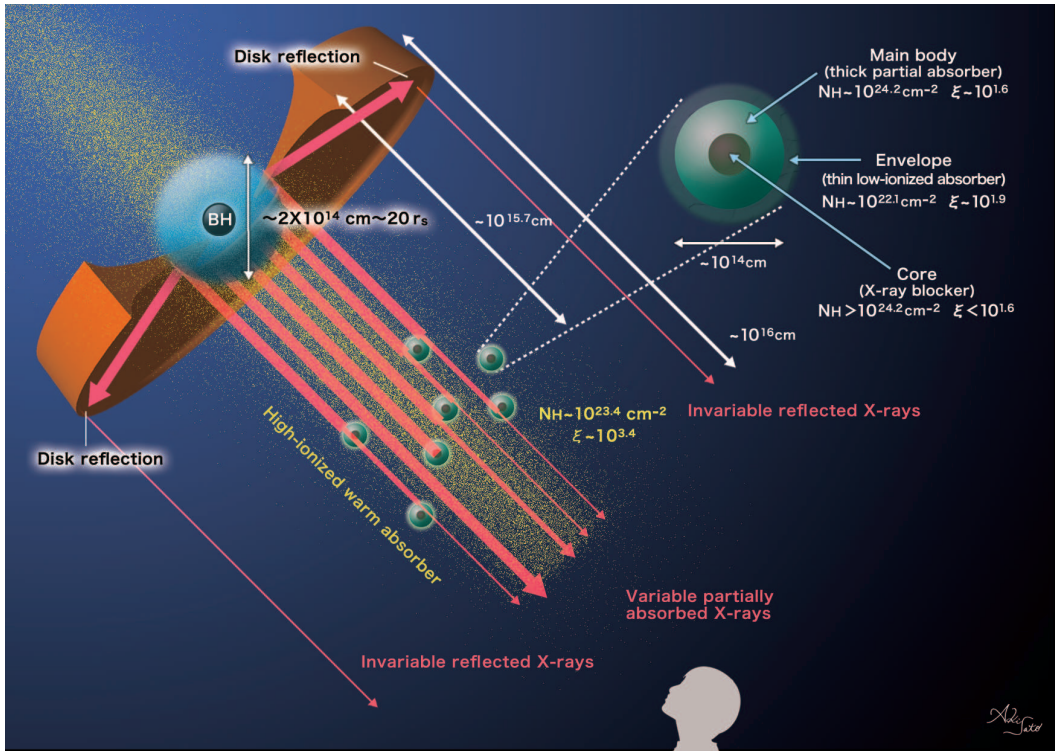


Fig. 12. Schematic picture of the variable partial covering model for MCG-6-30-15 and internal structure of the absorbing clouds.

NASA/Goddard Space Flight Center.

For data reduction, we used the software provided by the High Energy Astrophysics Science Archive Research Center (HEASARC) at NASA/Goddard Space Flight Center and Chandara X-ray Center (CXC) at Harvard-Smithsonian Center for Astrophysics. K.E. acknowledges Ms. Akiko Sato for helping us illustrate our model and producing a beautiful artwork.

References

- Arnaud, K. 1996, *Astronomical Data Analysis Software and Systems V*, A.S.P., Conference Series, 101, 17
- Blandford, R. D. 1990, in “Active Galactic Nuclei”, Saas-Fee Advanced Courses, volume 20, Springer.
- Balucinska-Church, M., & McCammon, D. 1992, *ApJ*, 400, 699
- Fabian, A. C., et al. 2002, *MNRAS*, 335, L1
- Fisher, K. B., Huchra, J. P., Strauss, M. A., Davis, M., Yahil, A., & Schlegel, D. 1995, *ApJS*, 100, 69
- George, I. M. & Fabian, A. C. 1991, *MNRAS*, 249, 352
- Grevesse, N., Noels, A., and Sauval, A. 1996, in “Cosmic Abundances” ASP Conference Series, 99, S. Holt and G. Sonneborn, eds.
- Guainazzi, M., et al. 1999, *A&A*, 341, L27
- Inoue, H., & Matsumoto, C. 2001, *AdSpR*, 28, 4451
- Inoue, H., & Matsumoto, C. 2003, *PASJ*, 55, 625
- Inoue, H., Miyakawa, T. & Ebisawa K., 2011, *PASJ*, 63, S669
- Ishida, M., Suzuki, K., & Someya, K. 2007, *JX-ISAS-SUZAKU-MEMO-2007-11*, 1
- Kallman, T. & Bautista, M. 2001, *ApJS*, 133, 221
- Kallman, T. R., Palmeri, P., Bautista, M. A., Mendoza, C., & Krolik, J. H. 2004, *ApJS*, 155, 675
- Laor, A. 1991, *ApJ*, 376, 90
- Magdziarz, P., & Zdziarski, A. A. 1995, *MNRAS*, 273, 837
- Matsumoto, C., Inoue, H., Fabian, A. C., & Iwasawa, K. 2003, *PASJ*, 55, 615
- Matsuoka, M. et al. 1990, *ApJ*, 361, 440
- McKernan, B. & Yaqoob, T. 1998, *ApJ*, 501, L29
- Miller, L., Turner, T. J. & Reeves, J. N. 2008, *A&A*, 483, 437
- Miller, L., Turner, T. J. & Reeves, J. N. 2009, *MNRAS*, 399, L69
- Miniutti, G., & Fabian, A. C. 2004, *MNRAS*, 349, 1435
- Miniutti, G., et al. 2007, *PASJ*, 59, 315
- Miyakawa, T. 2010, Doctoral Thesis, University of Tokyo, ISAS Research Note 852
- Miyakawa, T., Ebisawa, K., Terashima, Y., Tsuchihashi, F., Inoue, H., and Życki, P. 2009, *PASJ*, 61, 1355 (Paper I)
- Niedźwiecki, A., & Życki, P. T. 2008, *MNRAS*, 386, 759
- Niedźwiecki, A., & Miyakawa, T. 2010, *MNRAS*, 509, 22
- Reynolds, C. S. and Fabian, A. C., 1995, *MNRAS*, 273, 1167
- Reynolds, C. S., Fabian, A. C., Brenneman, L. W., Miniutti, G., Uttley, P., and Gallo, L. C., 2009, *MNRAS*, 397, L21
- Risaliti, G. et al. *MNRAS*, 2011, 410, 1027
- Tanaka, Y., et al. 1995, *Nature*, 375, 659
- Turner, T. J. & Miller, L. 2009, *Astron Astrophys Rev*, 17, 47
- Turner, T. J., Reeves, J. N. & Kraemer, S. B. & Miller, L. 2008, *A&A*, 483, 161
- Yaqoob, T. 1997, *ApJ*, 479, 184
- Young, A. J., Lee, J. C., Fabian, A. C., Reynolds, C. S., Gibson, R. R., & Canizares, C. R. 2005, *ApJ*, 631, 733
- Życki, P. T., Ebisawa, K., Niedźwiecki, A. and Miyakawa, T. 2010, *PASJ*, 62, 1185